Separation and Purification Technology 405 (2026) 138878

Contents lists available at ScienceDirect

Separation and Purification Technology

journal homepage: www.elsevier.com/locate/seppur

Modeling and process analytics as a basis for future predicting the dynamic behavior of a lab-scale vacuum belt filter

Volker Bächle *, Merlin Marvin Wolske, Stefan Schmidt, Marco Gleiß *

Karlsruhe Institute of Technology, Institute of Mechanical Process Engineering and Mechanics, Strasse am Forum 8, 76131 Karlsruhe, Germany

ARTICLE INFO

Editor Name: V Tarabara

Keywords:
Vacuum belt filter
Multi-compartment-model
Filtration
Optical detection

ABSTRACT

Real-time analysis and prediction of the process performance is a major challenge, as parameters such as e.g. cake porosity cannot be measured directly during filtration and the correlations between parameters are complex. In case of the example cake porosity the empirical correlation depends on particle size distribution, solids volume concentration, particle shape and pressure difference. As a result, it is calculated indirect through measurements of cake height and weight. Unknown changes to parameters in real systems are therefore only detectable in terms of the filtrate volume flow or filtration time. In this context, time-consuming and cost-intensive large-scale studies on the influence of the respective parameters are necessary. One approach is to introduce real-time analysis methods and a model to describe filtration. This paper presents, on the one hand, the implementation of an optical method using a camera to detect the transition between filtration and desaturation. On the other hand, it presents the detailed introduction of a multi-compartment model to describe filtration and desaturation on a lab-scale vacuum belt filter. Experiments have shown that only the bright-field method for optical detection can deliver reliable results as particles within the suspension scatters the light, too. For the filtration model a sufficiently fine spatial resolution of 7.6 mm (50 compartments) enables a realistic representation of the residence times, while too coarse discretization quickly leads to pronounced axial remixing, which does not occur in this form in real belt filters.

1. Introduction

Cake filtration is a widely used technology for separating solids from liquids and offers the possibility of mechanical dewatering. The driving force is an applied pressure difference between the top and bottom of a filter media that retains the solids particles on its surface. Continuous vacuum filters are continuous operation machine which use a vacuum pump to generate the applied pressure difference [1]. Due to the flexible machine design, this type of filter is applied in several industrial applications. Examples can be found in the pharmaceutical [2] and chemical industry or minerals processing [3]. Especially vacuum belt filters are applied in the chemical industry because they allow an efficient filter cake washing. Here, the estimation of the cake formation process is based on Darcy's law which allows to correlate pressure difference and filtrate flow for laminar conditions [4]. In the 1920s, Sperry introduced the concept of specific resistance, defined as the reciprocal of Darcy's permeability coefficient [5]. At the same time, he developed a method for determining the resistance [6]. Ruth examined the compressibility of filter cakes and its effect on fluid flow through filter media. He used an average specific cake resistance in his calculations and proved that Sperry's equations were mathematically equivalent to his [7]. Carman and Kozeny subsequently expressed the hydraulic resistance in the Darcy's equation by applying material-specific parameters based on the Sauter diameter, a porosity function [8,9]. After the fundamental equation for permeability through porous media Grace looked at the structure and performance of filter media which prevent penetration of particles while filtering [10,11]. This is followed by studies of the internal structures of filter cakes by Tiller and Shirato in the 1960s [12,13]. They looked into the porosity of filter cakes under constant pressure and introduced first mathematical approaches for compressibility. According to Tiller and Yeh, fine particles in the range below a characteristic particle size of 10 to 20 µm form highly porous structures through significant agglomeration, as interparticle surface forces outweigh the gravitational forces [14]. All of these approaches need an empirical basis to mathematically describe filtration devices and are therefore insufficient for describing and adapting to unknown conditions.

To increase efficiency, solutions are being explored in the industrial environment to enhance the efficiency of filtration devices. In addition

* Corresponding authors.
E-mail addresses: volker.baechle@kit.edu (V. Bächle), marco.gleiss@kit.edu (M. Gleiß).

https://doi.org/10.1016/j.seppur.2026.138878
Received 5 March 2026; Received in revised form 8 June 2026; Accepted 9 June 2026
Available online 13 June 2026

Symbols

Latin letters

a_0, a_1, a_2	Parameter for the fit function $I(x)$, –
a, b	Material-dependent fitting parameters for desaturation, –
A	Filter area, m^2
$A_{c,tr}$	Cross section of the filter cake, m^2
$\mathbf{A}(x,y)$	Matrix: Values of the optical image, –
B	Belt filter width, m
B_o	Blue value of the optical image from the camera, –
c_V	Solid volume concentration, %
d_{po}	Pore diameter, m
Δp	Pressure difference, Pa
Δt	Time step simulation, s
G_o	Green value of the optical image from the camera, –
GR	Gray value, –
h_c	Filter cake height, m
h_l	Height of liquid above filter cake, m
$\mathbf{I}(x)$	Matrix: Light intensity distribution of the optical image, –
$\widehat{\mathbf{I}}(x)$	Matrix: Normalized light intensity distribution, –
$I(x)$	Fit function through the light intensity distribution, –
K	Kinetics parameter for desaturation, –
L_c	Compartment length, m
L_{belt}	Belt filter length for filtration, m
m_c	Filter cake mass, Kg
m_l	Liquid mass, Kg
$\dot{m}_c$	Mass flow of formed filter cake, Kg s^{-1}
$\dot{m}_{c,tr}$	Mass flow of transported cake, Kg s^{-1}
$\dot{m}_{filt}$	Liquid filtrate mass flow, Kg s^{-1}
$\dot{m}_l$	Liquid mass flow, Kg s^{-1}
$\dot{m}_{l,dr}$	Liquid mass flow leaving the filter cake, Kg s^{-1}
n	Fit parameter, –
n_{it}	Number of iterations per compartment, –
N	Number of compartments, –
N_o	Number of pixels for the length of the belt filter, –
M_o	Number of pixels for the width of the belt filter, –
p_c	Filter cake permeability, m^2
$p_{c,rel}$	Relative filter cake permeability, m^2
$\bar{p}_k$	Capillary pressure, Pa
R_o	Red value of the image from the camera, –
S	Filter cake saturation, –
$S_i(t)$	Time dependent desaturation, –
S_r	Remnant saturation, –
S_∞	Equilibrium saturation, –
t	Time, s
V_c	Filter cake volume, m^3
V_l	Liquid volume, m^3
V_{po}	Pore volume, m^3
V_{tot}	Total volume of filter cake, m^3
$\dot{V}_{in}$	Feed volumetric flow, mL min^{-1}
$\dot{V}_l$	Liquid volumetric flow, m^3 s^{-1}
$\dot{V}_{l,dr}$	Liquid volumetric flow leaving the filter cake (desaturation), m^3 s^{-1}
$\dot{V}_{filt}$	Filtrate volumetric flow, m^3 s^{-1}
x	Coordinate for the length of the belt filter, –
$x_{50.3}$	Mass/volume related median diameter, µm
y	Coordinate for the width of the belt filter, –

Greek letters

α	Height specific cake resistance, m^{-2}
β	Filter media resistance, m^{-1}
γ	Surface tension water, N m^{-1}
ε	Cake porosity, –
η_l	Dynamic viscosity of the liquid, Pa • s
κ	Concentration parameter, –
ν_l	Transport velocity for liquid, m s^{-1}
ν_{tr}	Transport velocity of the belt, m s^{-1}
ρ_s	Solid density, Kg m^{-3}
ρ_l	Liquid density, Kg m^{-3}
τ	Residence time, s
v_{belt}	Belt speed, Mm min^{-1}
φ	Solids volume fraction, –

Abbreviations

CFD	Computational fluid dynamics
CFL	Courant Friedrichs Lewy number
ODE	Ordinary differential equations
PDE	Partial differential equation
RMSE	Root mean square error
TCP	Transmission control protocol

to the use of optimized device components, process analytics and modeling also contribute to an increase in efficiency. Today, enhanced computing power combined with efficient solution algorithms offers enormous potential and enables the development of innovative modeling strategies. This is particularly important when mathematical models will be used as the basis for model predictive control or the integration of soft sensors to predict the current state of the apparatus. [15,16]

The scientific basis of cake filtration for actual simulation was developed in the 1970s and 1980s. Filtration is based on a similar theoretical basis as thickening [17–20]. The mathematical analysis and application of numerical methods then took place in the 2000s [21–23]. These approaches mainly consider the liquid phase, since flow calculation in a filter cake is a common procedure and the compression of the pores in the solid phase is based on the same principles of thickening. Bürger et al. [24] subsequently extended the theory of sedimentation and consolidation to pressure filtration, while also taking into account the deformation and movement of the solid phase. According to Bürger et al. [24] the filtration is divided into five steps: cake formation, compression, dewatering, cake washing, and repeated cake dewatering, focusing on the first two steps. Stickland et al. [25] extended this approach for compressible filter cakes to vacuum filtration and examined the transition between cake formation, consolidation, and dewatering in a one-dimensional physical model. The one-dimensional approach was then extended to vacuum drum filters, whereby it was found that the filter cake in the dewatering zone tends to solidify at a lower flow stress than the capillary inlet pressure [26]. But even these approaches have the assumption of a homogeneous filter cake over the complete filter system.

Sauer et al. [27–29] model inhomogeneities in the filter cake height and validated simulation results with experimental data. These models take physical aspects into account, but are unsuitable for real-time analysis and predictions due to the high computational effort required. To achieve this, a reduced model for filtration is necessary. This has already been examined in detail for solid bowl centrifuges [30–33]. For vacuum belt filters Boiocchi et al. [34] introduced a model which describes the filtration process in more detail with mesh sizes of 350 µm in their case, but is also not real-time capable. Currently, there is a lack of real-time capable process models for vacuum belt filters to predict process behavior and enable process optimization. Real-time simulation has the decisive advantage of making an important contribution to the development of digital process twins to achieve

autonomous operation in the future using adaptive model predictive control strategies.

The aim of this work is to develop a mathematical model for calculating the dynamic process of a vacuum belt filter, which will later serve as the basis for an adaptive control strategy. To this end, we present a multi-compartment model, which allows to predict the filter cake formation process and subsequent mechanical desaturation. Therefore, the mathematical model divides the vacuum belt filter into different zones to consider the behavior of the filter cake due to cake formation and desaturation by gas differential pressure. The validation is based on different experiments for calcite suspensions. Therefore, we implemented different measurement methods on the vacuum belt filter. A camera system detects the transition between cake formation and cake desaturation based on the total internal reflection. Additionally, a laser is used to determine the cake height at the end of the filter device to estimate the porosity of the filter cake.

2. Modeling vacuum belt filter

Vacuum belt filters involve continuous processes in which the cake height and saturation change over time. A suitable way to model the temporal and spatial change on the filter apparatus is the use of a multi-compartment model. This simplifies the mathematical formulation to ordinary differential equations (ODE). The use of ODEs simplifies the system of equations and allows for a simpler numerical calculation of the coupled equation system. This is particularly important in the context of integrating mathematical models into model predictive control to achieve dynamic optimization during the determination of the control variables with the greatest possible computational efficiency.

Fig. 1 shows the multi-compartment model of the investigated lab scale vacuum belt filter. Two zones are used for modeling. In the cake formation zone, the suspension is fed onto the belt filter via the inlet. Subsequently, in the operation of the belt filter a vacuum is applied on the bottom of the filter medium, resulting in a pressure difference to the top, causing the suspension to flow towards the filter medium. The filter medium has the task of restraining the solid particles which generate particle bridges and form filter cake and producing a filtrate that is as pure as possible. Thus, filter cake formation takes place due to an applied gas differential pressure.

The following assumptions were made for the mathematical modeling of cake formation and mechanical dewatering.

1. The particles are significantly smaller than the apparatus, which allows for macroscopic modeling.
2. The suspension feed leads to a homogeneous distribution of the suspension on the filter medium. Segregation effects within the suspension are not considered (ideal back-mixing which leads to no concentration gradient of solids in the first and every subsequent suspension compartment)
3. All particles are in the same shape and density.
4. The particles and the fluid are incompressible. In the dewatering zone, gas and liquid flows within the filter cake are independent and must be calculated separately. It is important to realize that gas flow is only a consequence of pore desaturation through gas differential pressure, not the cause [1]. In this work, only the liquid phase is balanced, rendering the compressibility of the gas phase irrelevant.
5. The filter cake builds up evenly on the filter belt. No segregation along the filter belt width.
6. Cake formation process can be described according to Darcy.
7. The filter cake has a constant porosity. The filter cake behaves in an incompressible manner.
8. Mechanical undersaturation occurs purely through gas differential pressure filtration after the capillary entry pressure has been exceeded.

In contrast to a CFD model, the multi-compartment model does not take flow behavior into account but approximates the inflow using an average flow velocity derived from the volume flow.

2.1. Material functions

Material functions include filtration properties to describe the cake formation process and mechanical desaturation of the filter cake. According to our assumptions, ideal back-mixing occurs in the compartments, thus neglecting sedimentation of particles which results in a non-uniform cake formation process.

On a belt filter, the driving force for cake formation is the pressure difference of 0.5 bar caused by an applied vacuum. For systems with very fine particles, a compressible filter cake may form. According to Tiller and Yeh compressible filter cakes occur with particle sizes smaller than 10 µm to 20 µm [14]. The used particles are smaller, which assures that this filter cake has at least a slight compression. Compression shows its difficult filtration behavior with changing pressures and cake heights. In this work the pressure difference stays around 0.5 bar in our belt filter device and the cake heights will stay in the range between 1 mm and 2 mm, as the filtration time is limited. The specific cake resistance α to describe the resistance of the porous filter cake is measured with exactly these parameters. Therefore, α include the compression and porosity at this parameter set and is used as a constant value throughout this work. Bourcier et al. [35] introduce a model to describe the influence of particle size and shape on the compressibility and validated it experimentally. Additionally, the assumption of a homogenous formed filter cake with a constant porosity is used to calculate the cake formation process. The porosity and cake resistance are determined experimentally as shown in Table 1.

With pressure differences greater than the capillary entry pressure, gas invades the saturated filter cake and replaces liquid, resulting in dewatering. Capillary pressure depends on pore size, causing the largest pores to be drained first. Liquid is then only present within smaller pores and joints with decreasing liquid saturation. As a result, the liquid flow

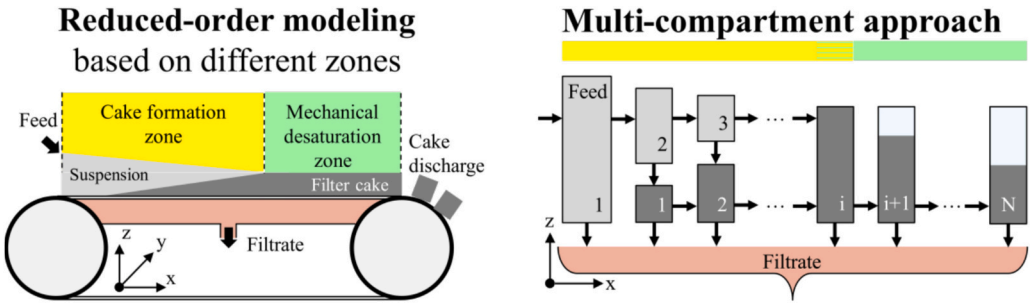

Fig. 1. Schematic figure of the multi compartment approach for the belt filter with the two zones for cake formation and desaturation. On the left side is a schematic figure of the vacuum belt filter and on the right is the discretisation. The coordinate system describes the position on the belt filter, where x represents the belt length, y the belt width, and z the height of the slurry/cake.

Table 1
Summary of constant (top) and varied (bottom) model parameters for simulation and experiments.

Name	Value	Unit	Determination
Constant parameters			
Belt filter width B	0.06	m	Experimental setup
Belt filter end position L_{belt}	0.38	m	Experimental setup
Pressure difference Δp	$0.5 \cdot 10^5$	Pa	Measurement filter
Capillary pressure $\overline{p}_k$	$0.2 \cdot 10^5$	Pa	Young-Laplace Eq. (22)
Spec. Cake resistance α	$4.1 \cdot 10^{14}$	m^{-2}	Measured acc. [41]
Filter medium resistance β	$9.0 \cdot 10^{11}$	m^{-1}	Measured acc. [41]
Porosity ε	0.55	–	Measured gravimetrically
Equilibrium saturation S_∞	0.38	–	Fit parameter
Solid density ρ_s	2600	Kg m^{-3}	Literature [46]
Liquid density ρ_l	998	Kg m^{-3}	Literature [46]
Dynamic viscosity η_l	$1.002 \cdot 10^{-3}$	Pa s	Literature [46]
Varied parameter range in experiments and simulations			
Number of compartments N	5–1000	–	
Compartment length L_c	L_{belt}/N	m	
Feed volume flow $\dot{V}_{in}$	30–50	mL min^{-1}	
Belt speed v_{belt}	100–300	Mm min^{-1}	
Solid volume concentration c_V	10–20	%	

rate continues to decrease and equilibrium saturation is achieved through a balance of forces between the pressure difference and the capillary pressure. Here, it is assumed that the pore size distribution in the filter cake is constant. The relative specific liquid permeability $p_{c,rel}(S)$ starts at 1 (100%) and $S = 1$ (100%), when all pores in the filter cake are still fully saturated. This correlates with single-phase liquid flow. Eq. (14) becomes zero at the mechanical limit of desaturation S_r, where no more liquid movement is possible [36].

Sauer et al. [29] demonstrate the use of the concept of relative permeability according to Brutsaert [36] and capillary pressure distribution for the desaturation of non-uniform filter cakes at a pressure of 0.5 bar. This approach also represents the necessary material functions for describing desaturation with the dynamic model presented in this work.

2.2. Control volume and discretization

The description of the dynamic process behavior of the continuously operating vacuum belt filter is based on the calculation of dynamic mass balances for each interconnected compartment. In the cake formation zone, the liquid mass balance for compartment i is calculated as follows:

$$\frac{dm_{l,i}}{dt} = \dot{m}_{l,i-1} - \dot{m}_{l,i} - \dot{m}_{filt,i}. \tag{1}$$

Here, $m_{l,i}$ is the liquid mass, $\dot{m}_{l,i-1}$ is the ingoing liquid mass flow, $\dot{m}_{l,i}$ is the outgoing liquid mass flow and $\dot{m}_{filt,i}$ is the liquid filtrate mass flow. All variables are located to compartment i. The transformation of Eq. (1) to a volume balance allows directly the calculation geometric parameters of the liquid zone and the filter cake. Therefore Eq. (1) is extended to a volume balance:

$$\frac{d(\rho_l V_{l,i})}{dt} = \rho_l \dot{V}_{l,i-1} - \rho_l \dot{V}_{l,i} - \rho_l \dot{V}_{filt,i}. \tag{2}$$

In this case, ρ_l is the liquid density, $\dot{V}_{l,i-1}$ and $\dot{V}_{l,i}$ are the ingoing and outgoing liquid volumetric flow and $\dot{V}_{filt,i}$ is the filtrate flow of compartment i. With the assumption of a constant liquid density and a rectangular shaped filter cake Eq. (2) becomes the following expression:

$$\frac{dV_{l,i}}{dt} = h_{l,i}\, B\, v_{l,i} - h_{l,i-1}\, B\, v_{l,i-1} - \dot{V}_{filt,i}. \tag{3}$$

Here, $h_{l,i}$ is the height of the liquid above the filter cake and $v_{l,i}$ describes the belt speed. The filtrate volumetric flow $\dot{V}_{filt,i}$ can be derived from Darcy's law:

$$\dot{V}_{filt,i}(t) = \frac{A \bullet \Delta p}{\eta_l(\alpha \bullet h_{c,i}(t) + \beta)}. \tag{4}$$

Here, A is the filter area which is constant for each compartment, B is the filter belt width, Δp is the applied gas differential pressure between the bottom and the top of the filter, η_l is the dynamic viscosity of the liquid, α is the height specific cake resistance, β is the filter media resistance, $h_{c,i}(t)$ is the temporal changing filter cake height in compartment i. A mass balance for the filter cake is also necessary to describe the filter cake formation process:

$$\frac{dm_{c,i}}{dt} = \dot{m}_{c,tr,i-1} - \dot{m}_{c,tr,i} + \dot{m}_{c,i}. \tag{5}$$

Here, $m_{c,i}$ is the accumulated mass of the filter cake in compartment i, $\dot{m}_{c,tr,i-1}$ and $\dot{m}_{c,tr,i}$ is the ingoing and outgoing filter cake mass flow rate due to the belt transport of the filter cake and $\dot{m}_{c,i}$ is the mass flow of formed filter cake. Eq. (5) can be transformed to a volume balance to calculate directly the filter cake volume:

$$\frac{d(V_{c,i})}{dt} = A_{c,tr,i-1} v_{tr,i-1} - A_{c,tr,i} v_{tr,i} + \kappa\, \dot{V}_{filt,i}. \tag{6}$$

With $A_{c,tr\,j-1}$ and $A_{c,tr,i}$ as the cross section of the filter cake on the filter belt, $v_{tr,i}$ is the transport velocity of the belt and κ is a concentration parameter which depends on feed solids volume fraction φ and filter cake porosity ε which allows to correlate the filtrate volumetric flow with the filter cake volumetric flow. Particle loss through turbidity of the filtrate is neglected. The concentration parameter κ in Eq. (7) relates the cake volume to the separated liquid volume. This parameter can also be described with the solid concentration volume c_v and the cake porosity ε, which represents the relative void volume in the cake and thus the relative amount of liquid, if all voids are completely filled with liquid.

$$\kappa = \frac{h_{c,i}(t) \bullet A}{\dot{V}_{filt,i}\,(t)} = \frac{c_v}{1 - c_v - \varepsilon} \tag{7}$$

After cake formation and drainage of the excess liquid through the filter cake, the filter cake becomes undersaturated during gas differential pressure because the capillary inlet pressure is exceeded. This process is included in the dynamic model by solving a mass balance for the liquid in the mechanical dewatering zone of the vacuum belt filter:

$$\frac{dm_{l,i}}{dt} = \dot{m}_{l,i-1} - \dot{m}_{l,i} - \dot{m}_{l,dr,i}. \tag{8}$$

In Eq. (8) $m_{l,i}$ is the liquid mass in the porous filter cake, $\dot{m}_{l,i-1}$ and $\dot{m}_{l,i}$ are the ingoing and outgoing mass flow rates due to the transport of the filter cake and $\dot{m}_{l,dr,i}$ is the liquid mass flow leaving the filter cake due to cake desaturation. An important factor in describing mechanical dewatering of filter cakes is the saturation S of the pore system. The saturation describes the ratio of liquid volume V_l to pore volume V_{po}:

$$S = \frac{V_l}{V_{po}} = \frac{V_l}{\varepsilon \bullet V_{tot}}. \tag{9}$$

In addition, the liquid volume can be replaced by the saturation S, total volume of the filter cake $V_{tot.}$ and porosity ε:

$$V_l = S \bullet \varepsilon \bullet V_{tot.} \tag{10}$$

Inserting Eq. (10) into Eq. (8) yields the following expression:

$$\frac{dS_i}{dt} = \frac{1}{\varepsilon \bullet V_{tot,i}} \bullet \left[\varepsilon \bullet (S_{i-1}\dot{V}_{i-1} - S_i \dot{V}_i) - \dot{V}_{l,dr,i}\right]. \tag{11}$$

Here, $\dot{V}_{i-1}$ and $\dot{V}_i$ are the volumetric flows of the transported filter cake, S_{i-1} and S_i are the saturation of the ingoing and outgoing filter cake and $\dot{V}_{l,dr,i}$ is the volumetric flow of liquid which leaves the filter cake due to desaturation. Eq. (11) allows to directly calculate the saturation of the filter cake along the horizontal position along the filter belt in the dewatering zone. Additionally, it was assumed that the filter cake had a homogeneous structure and therefore a constant height and porosity. The volumetric flow of the transported filter cake is calculated by assuming a rectangular shape of the filter cake:

$$\dot{V}_i = v_{tr,i} \bullet A_{c,tr,i.} \tag{12}$$

A simplified model that takes physical influencing factors into account is required to describe the desaturation process of the cake on filter belt. Here, Anlauf et al. [1] defined a model to describe the filtrate volumetric flow during the desaturation based on the following formulation:

$$\dot{V}_{l,dr,i} = \frac{2\,A \bullet p_c \bullet p_{c,rel,i}(S)}{\eta_l} \bullet \frac{\Delta p - \overline{p}_k}{h_{c,i}(t)}. \tag{13}$$

It is important to note that A is the filtration area of compartment i, p_c is the filter cake permeability of a fully saturated filter cake with $S = 1$, $p_{c,rel}(S)$ is the relative filter cake permeability which occurs due to the undersaturation of the pore space, Δp is the applied vacuum pressure difference and $\overline{p}_k$ is the average capillary pressure. The relative permeability can be determined using an empirical approximation according to Brutsaert [36].

$$p_{c,rel,i}(S) = \left(\frac{S_i(t) - S_r}{1 - S_r}\right)^n, n > 0 \tag{14}$$

S_r describes the limit of mechanical desaturation and $S_i(t)$ is the time-dependent desaturation. The parameter n is a fit coefficient that describes the steepness of the function. Since desaturation only takes place within the dewatering zone, this must be checked iteratively by means of a logical query.

The Eqs. (13) and (14) are enough to close the volume balance for cake desaturation in this work. To further describe the desaturation kinetic as a whole, a correlation between the saturation degree S and the filtrate volume flow at the cake outlet $\dot{V}_{l,dr}$ for constant porosity ε and liquid density ρ_l can be formulated:

$$A \bullet h_c \bullet \varepsilon \bullet \frac{\mathrm{d}S}{\mathrm{d}t} = -\dot{V}_{l,dr}. \tag{15}$$

Now both Eqs. (13) and (14) have to be interrelated to Eq. (15) and integrated for the initial condition of $t_2 = 0$ and $S = 1$. Precondition for the validity is the possibility to reach $S = S_r$ with the applied pressure difference. To fulfill this condition, Δp has to be much greater than $\overline{p}_k$. In real applications of vacuum filtration the mechanical limit of desaturation S_r cannot be achieved. To solve this problem, Eq. (14) is related to the corresponding equilibrium saturation S_∞ for each particular pressure difference. With two material-dependent fitting parameters a and b, as well as a kinetics parameter K the Eqs. (16) and (17) are formulated. The kinetic parameter K contains all relevant influencing parameters. This also represents the method to describe the saturation S according to VDI guideline 2762–3. [1,37]

$$\frac{S - S_\infty}{1 - S_\infty} = [1 + a \bullet K]^{-b} \tag{16}$$

$$K = \frac{p_c \bullet (\Delta p - \overline{p}_k)}{\varepsilon \bullet \eta_l \bullet h_c^2} \bullet t_2 \tag{17}$$

3. Advanced process analytics and monitoring

Process analytics is implemented to assess the state of filtration in terms of both filter cake formation and cake dewatering. For this purpose, a camera system is used to evaluate the surface of the filter cake in total reflection to draw conclusions about the end of the cake formation process and the start of cake dewatering to calibrate the compartment model and estimate the current dewatering behavior of the material. Additionally, laser measurements allow us to estimate the filter cake height for evaluating the filter cake porosity based on a mass balance for the vacuum belt filter. Using laser triangulation to determine the cake height are done by Hamachi et al. and Haenecke who prove the feasibility of accurately measuring in-situ powder thicknesses [38,39]. The implementation of the measuring equipment is shown schematically in Fig. 2.

3.1. Optical filtration characterization

An optical method is used to distinguish between the two zones. This method must be able to determine the position of the transition on the belt filter. After this position, the equations for calculating the compartments change. For this purpose, an elongated light source is attached along the entire length of the belt filter and a camera is used for recording (see Fig. 2). Depending on the surface texture, different observations are made. On a smooth surface, all light beams incident from one direction are reflected at the same angle (specular reflection). If the surface is rough, the light from one direction of incidence are reflected in many different directions. Due to scattering, no reflection can be observed (diffuse reflection). Filtration shows a transition here. When the filter still contains liquid, the surface appears smooth due to surface tension. Conversely, the filter cake has a rough surface due to its particulate composition. [40]

This paper presents and compares the two methods of bright-field illumination and dark-field illumination. In bright-field illumination, the camera and light source are aligned in an angle of specular reflection. In dark-field illumination, the camera is positioned outside the reflection of the light source, orthogonal to the belt filter surface. This means that only scattered light (diffuse reflection) enters the camera. To avoid unwanted scattering and false detections, a light source that is as directional as possible is used. [40]

Both methods aim to detect the transition from cake formation to cake desaturation. At the boundary, the change from specular to diffuse reflection causes a sudden change in the light intensity detected by the camera. To evaluate this signal on the camera, the following steps are performed: image input, gray value conversion, mean value calculation, smoothing, normalization, and edge detection. When the image is imported, a color image is stored in a matrix $\mathbf{A}(x, y)$ with dimensions $M_o \times N_o \times 3$. With the coordinates: $x \in \{1, \ldots, N_o\}$ (length of the belt filter), $y \in \{1, \ldots, M_o\}$ (width of the belt filter) and with M_o and N_o as the number of pixels in the image. For each position in the two-dimensional image, a vector with three entries is stored: red R_o, green G_o, and blue value B_o. In the second step, the color image is converted into a grayscale image according to Eq. (18). The dimension of $\mathbf{A}(x, y)$ is thus reduced to $M_o \times N_o$ with GR as the value.

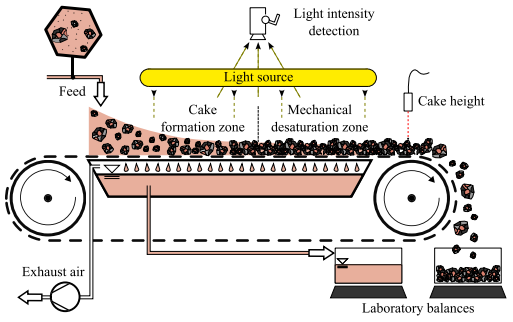

Fig. 2. Schematic diagram of the vacuum belt filter with integrated sensors for determining process parameters.

$$GR = 0.299 \bullet R_o + 0.587 \bullet G_o + 0.114 \bullet B_o \tag{18}$$

In the third step, the dimension is further reduced to a $1 \times N_o$ matrix, since only the position along the belt filter is relevant for the calculation. To avoid losing any information about the filtration edge, an average is calculated along the y-axis (width of the belt filter) using Eq. (19). Here, $\mathbf{I}(x)$ represents the intensity value along the belt filter. However, averaging results in a more gradual transition of light intensity at the transition point.

$$\mathbf{I}(x) = \frac{1}{M_o} \sum_{y=1}^{M_o} \mathbf{A}(x,y) \quad \forall x \in \{1, \ldots, N_o\} \tag{19}$$

The light intensity obtained from averaging is smoothed in the next step. This compensates local fluctuations. These can be amplified, particularly when deriving the intensity directly, and thus lead to measurement errors. Smoothing is performed using SciPy's convolve1d() function and an interval width of 50 data points. The smoothed intensity distribution $\mathbf{I}(x)$ is normalized to its maximum $\max(\mathbf{I}(x))$:

$$\widehat{\mathbf{I}}(x) = \frac{\mathbf{I}(x)}{\max(\mathbf{I}(x))} \quad \forall x \in \{1, \ldots, N_o\}. \tag{20}$$

This step facilitates the comparability of different images. Along this normalized one-dimensional matrix $\widehat{\mathbf{I}}(x)$, the edge can now be determined using a gradient filter. This determines the position of the maximum gradient in the intensity distribution, which represents the transition point after the filtration. Mathematically, this is done using a derivation. One option is to directly derive the intensity values of $\widehat{\mathbf{I}}(x)$ by linearizing between the individual data points. However, this carries the risk of incorrect edge detection due to noise in the measurement signal of individual pixels. Therefore, another option is to fit the data points using a function of the intensity distribution $I(x)$, according to Eq. (21). For the intensity of the brighter area, the normalization applies values of $I(x) \approx 1$.

$$I(x) = 1 + \frac{a_0 - 1}{1 + e^{-a_1(x - a_2)}} \tag{21}$$

The selected function $I(x)$ always converges towards the value 1 on one side. Parameter a_0 describes the intensity on the darker side, parameter a_2 determines the center point of the edge on the x-axis. The higher the value of the parameter a_1, the sharper the edge in the function. The sign of a_1 determines whether the edge is sloping or rising. Initial values are required for the iteration of the regression of all data points at $\widehat{\mathbf{I}}(x)$. A positive value less than 1 should be selected for a_0. For a_1 the selected sign must be adapted to the method. In the bright field method, there is a decreasing intensity curve and a_1 is therefore positive, or negative for the dark field method. A positive value is selected for a_2. This allows both the expected behavior of bright field illumination and that of dark field illumination to be described. The parameters a_0, a_1, a_2 also provide a description of the boundary transition, which is important for monitoring filtration. A high value of a_1 therefore means an elongated transition and thus an inhomogeneous suspension distribution at the inlet of the belt filter. This results in an inhomogeneous filter cake and thus different filtration speeds across the width of the belt filter.

3.2. Experimental and simulation setup

Fig. 2 shows the schematic design of the lab-scale vacuum belt filter. The suspension is fed onto the filter belt at a defined flow rate between 30 and 50 mL min^{-1} using a CR 240 peristaltic pump from Verder Deutschland GmbH & Co. KG (Haan, Germany) and transported and filtered through a 07–1500-SK 011 filter fabric with a pore size of 11 µm from Sefar AG (Heiden, Switzerland). A DC motor from RS Components GmbH (Frankfurt am Main, Germany) is used to drive the filter belt, which can be controlled with 0–30 V for speed regulation. The filter fabric can thus move at a speed of up to 300 mm min^{-1}. The filtration distance on the belt filter is 380 mm. This corresponds to a minimum residence time of the suspension on the belt filter of 76 s. At the end of the belt filter, the filter cake is removed for gravimetric determination of the residual moisture. Drying takes place in a drying oven at 100 °C. All parameters used for simulation and experiments are summarized in Table 1. The measurements according to [41] are part of the *supplementary information*. For desaturation, the capillary inlet pressure and the average capillary pressure are important. In bridging theories, the $x_{90.3}$ value of the cumulative particle size distribution curve of the bridging agent is typically matched to the maximum pore throat diameter of the formation [42]. For the particle system used, this diameter is $x_{90.3} = 34.8$ µm. To calculate desaturation, we assume an average pore throat diameter d_{po} double the particle diameter. Using the Young-Laplace eq. (22) with a completely water-wet mineral ($\cos\theta \approx 1$) and a surface tension γ of water at 20 °C of 0.072 N m^{-1} [43], the capillary pressure $\bar{p}_k$ in Table 1 can be calculated. In real filter cakes, pore throat diameter depends on particle shape and distribution. Therefore, it must be measured in capillary pressure curves for each individual case to get exact values. This will be done in further research.

$$\bar{p}_k = \frac{4\gamma\cos\theta}{d_{po}} \tag{22}$$

To determine the parameters for the in-situ measurements on the belt filter, a laser distance sensor ILD1220–25 from MICRO-EPSILON MESSTECHNIK GmbH & Co. KG (Ortenburg, Germany), a Canon EOS M6 Mark II camera from Canon Deutschland GmbH (Krefeld, Germany) with an EF-M 14-45 mm F3.5–6.3 IS STM lens, and a 6202BCE-1S balance from Sartorius AG (Göttingen, Germany) are used. The laser distance sensor is a point measurement with a measuring rate of 1 kHz which is averaged for 1 s in the middle of the belt width for the cake height and the balance is for the filtrate quantity. A measurement to validate the usage of a single-point measurement is part of the *supplementary information*. In addition to the camera, a TUBEKITLED06 8.6 W/840230 V G5 light source from Ledvance GmbH (Munich, Germany) is installed. The pressure difference to the ambient pressure is measured using a PAA-21Y piezoresistive pressure transmitter from KELLER Druckmesstechnik AG (Winterthur, Switzerland).

Anhydrite with the product name TREFIL 1313–100 from Quarzwerke GmbH (Frechen, Germany) is used as the model particle. Anhydrite consists chemically of $CaSO_4$ and has a median particle diameter at a cumulative volume fraction of $x_{50.3} = 6.48$ µm, determined by laser diffraction spectroscopy on an LBS Helos Quixel from Sympatec GmbH (Basel, Switzerland). For all experiments, a suspension of anhydrite and deionized water with a solids volume fraction between 10% and 20% is used. Image analysis is performed entirely in Python. The NumPy, SciPy, and OpenCV packages are used [44,45]. The interface between the sensor technology and the computer is provided by Labview. Additionally, communication between Labview and Python based on the Transmission Control Protocol (TCP) is integrated. The clock rate set for recording the measurement signals and changes in the input variables is 0.4 s.

4. Results and discussion

4.1. Validation of the optical filtration characterization

Both bright-field and dark-field illumination methods are expected to be suitable for detecting the transition between the two zones. Fig. 3 shows the intensity distributions of the two methods side by side in an experiment with an initial solids volume fraction of $c_V = 10$ vol%. With bright-field illumination, the edge is clearly visible in the image. The intensity distribution shows the expected decrease in light intensity at the transition from suspension to filter cake. The edge is not a clear uniform front, but a transition zone in itself. The broadness of the signal change describes therefore the width of the transition zone. Within the

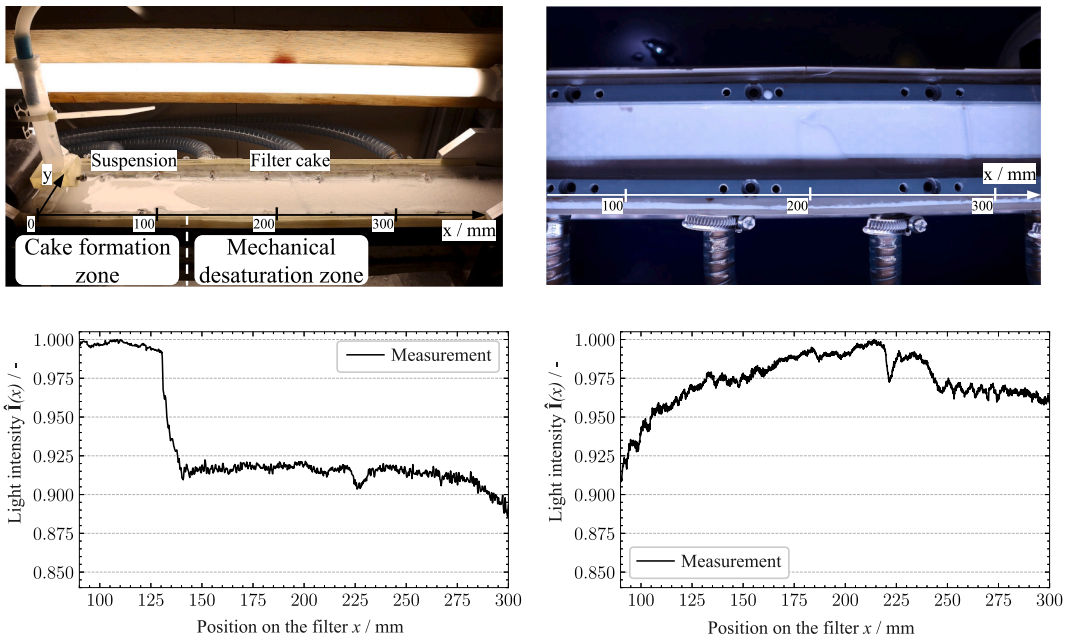

Fig. 3. Comparison of the bright field method (left) with the dark field method (right) as a snapshot from the camera and in evaluated form without smoothing (below the images).

model there is a single transition point for calculation needed, which is the reason for finding the bending point. In contrast, with dark field illumination, the edge is barely visible in the image. The intensity distribution also does not show the expected shape. This is due to the high solid concentration of the suspension of 10 vol %. The particles in the suspension scatter the light, resulting in a brightness comparable to that observed in the filter cake area. Lower concentrations could increase the intensity transition. However, higher feed solids volume fractions are more common in mining (initial solid mass content ranging from 25% to 45%), which is why lower concentrations are not considered further [47]. Dark field illumination is therefore not suitable for the measurement. In the following, only the bright field method will be considered.

The edge can now be determined using bright field illumination. To do this, the graph (Fig. 3, left) is smoothed and then the position of the transition point is determined using a gradient filter. According to Fig. 4, the smoothed intensity still shows fluctuations, which can be recognized as local extrema in the direct derivative. The measurement method developed here assumes that the filtration transition is more pronounced than the other fluctuations in the light distribution. The derivative will therefore have the highest value at its position. To identify it, the global extremum of the derivative is sought. If the fit (Fig. 4, right) is used, the global extremum can also be determined. This has the additional advantage that the derivative of the selected function has only one extremum. However, due to the construction of the function, the parameter corresponds exactly to the position of the extremum. This means that this step of the derivative is not necessary. Fig. 4 shows the two methods used to identify the filtration edge side by side. In the intensity distribution, there is a drop in light intensity of almost 10% at the location of the filtration edge. This is localized by both the direct method and the fit. It can be seen that the assumption of the global extremum in the direct method is justified.

However, Fig. 4 only shows a comparison in a snapshot. To better reflect practical application, position detection is performed with continuous filtration and changing zone transitions on the belt filter. Fig. 5 shows the progression of the filtration edge in a video sequence during filtration over time. To create a moving edge, the belt speed has been suddenly reduced by 10%. With this change the transition point will move to the new steady-state. This allows us to describe the effect of changes in the steady state on the measurement of the edge. In the left diagram, the video sequence is determined by direct derivation and shows jumps in edge detection of up to 10 mm between two measuring points. In the right-hand diagram, the identical video sequence is evaluated using the regression of Eq. (21). Here, the differences between the individual measuring points are a maximum of 0.5 mm. Both methods therefore lead to usable measurement results for the simulation, as the deviation is within a range of 5%. However, the direct method shows smaller jumps in the progression and returns slightly different values for the position. Due to the direct derivation method, differences from the

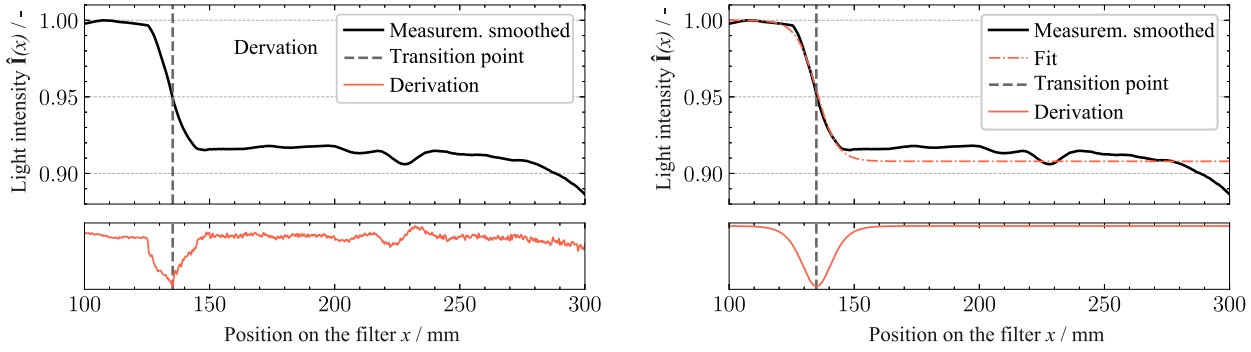

Fig. 4. Determination of the transition position by direct derivation on the left and fit according to Eq. (21) on the right using the bright field method.

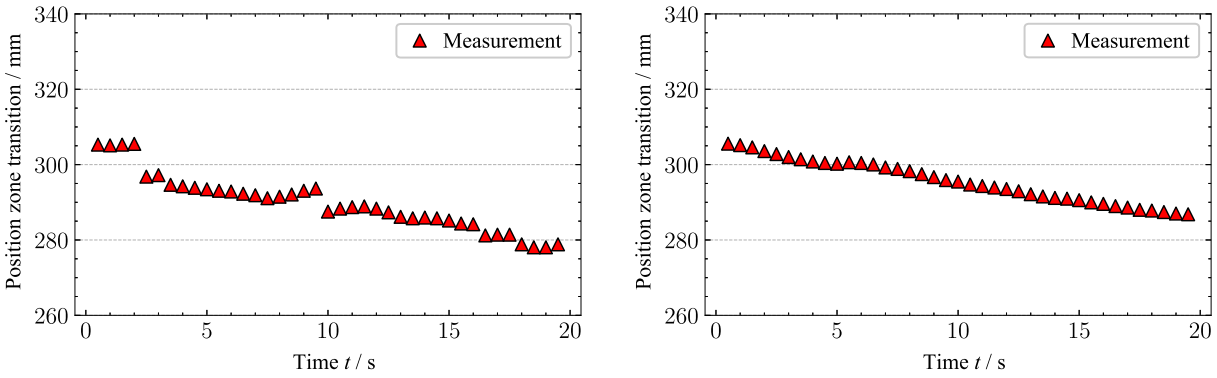

Fig. 5. Movement of the transition point over time with direct derivation on the left and fit according to Eq. (21) on the right.

perfect edge shape are more significant. They ensure that the maximum of the derivation is not hit exactly in the middle. The jumps are not observed due to the idealization of the transition point in the fit method. In addition, regression has the advantage that differences in the results occur less frequently. By adjusting a given function, an assumption is made about the course of the light intensity. If this course is not recognizable in the data, the fit fails. This results in an error that can be detected. With the direct method, on the other hand, an extremum can be found even for functions without a clear edge. This means that incorrect results are more likely to occur. However, the advantage of the direct method is that it requires less computing power. Calculating a numerical derivative is less complex than fitting a function with three parameters. In principle, both direct derivation and fitting to a given function are suitable for continuously recording the zone transition point between cake formation and mechanical desaturation. This allows optical edge detection to serve as input for the simulation.

4.2. Numerical effort for real time simulations

To be a basis for adaptive control strategy, the real-time capability of the dynamic model is a key factor. Unlike pure offline simulations, the model must be solvable in an efficient manner that the calculation can be performed within the available computing time and the results can be used immediately for future dynamic optimization. The goal is therefore to achieve sufficient model quality with reasonable numerical effort. The model structure of the vacuum belt filter is a multi-compartment model with N spatially discretized compartments. The spatial resolution can be easily scaled by increasing the number of compartments. The temporal discretization can be adjusted independently by varying the step size of the numerical differential equation solver. The temporal and spatial resolution of the model are coupled by the Courant Friedrichs Lewy number (CFL) [48]:

$$\mathrm{CFL} = \frac{v_{belt} \bullet \Delta t}{L_c} \leq 1. \tag{23}$$

It describes the numerical stability for convection-dominated transport processes. If the boundary value of 1 is exceeded, the numerical solution can become unstable since the information spreads over more than one spatial cell within a time step. With a CFL number limit of 1, increasing the number of compartments and thus a finer spatial resolution L_c requires a correspondingly smaller time step size Δt to ensure the stability of the numerical solution. Another significant factor influencing the numerical effort is the simulation time. The maximum relevant simulation duration can be the residence time τ on the belt filter. This is calculated from the belt speed v_{belt} and the length of the filter belt L_{belt}:

$$\tau = \frac{L_{belt}}{v_{belt}}. \tag{24}$$

The number of iterations n_{It} per compartment is then calculated from the residence time τ and time step size Δt:

$$n_{It} = \frac{\tau}{\Delta t}. \tag{25}$$

For each of the N compartments, three state variables must be calculated, which are described by three coupled differential equations. These include the suspension height, the cake height, and the saturation of the filter cake. The number of ODEs to solved therefore grows linearly with the number of compartments. In compliance with the CFL stability condition, the time step size must be reduced as the spatial resolution increases. With a constant simulation horizon, this leads to a proportional increase in the number of simulation steps required. In combination with the linearly increasing number of states, this results in a quadratic complexity for the simulation, depending on the number of compartments. Coarse spatial discretization can result in the transport velocity of the belt being modeled faster than the actual velocity. A further assumption is that the transport through each compartment is without time delay and homogeneously (ideal pipe reactor), whereby a corresponding distance is represented numerically in a shortened form.

Fig. 6 shows the response functions for a selected operating point with different numbers of compartments. A step change in belt speed from 300 mm min^{-1} to 100 mm min^{-1} was specified as the excitation. An increase in the number of compartments leads to a sharper sigmoid curve of the response function during the transition to a new steady-state operating point. The literature describes that with an increasing number of ideal back-mixed compartments in a cascade, the dynamic behavior increasingly corresponds to that of an ideal tubular reactor, since the axial back-mixing is reduced and the concentration gradient is modeled more sharply. A sharper transition of the response function is therefore characteristic of a tube reactor-like system [49].

With fewer compartments, simulations show a longer settling time until the new stationary operating point is reached. To estimate the required prediction horizon, the time span between the applied step change and the steady-state must therefore be determined. Since the residence time depends directly on the belt speed, it is advisable to perform this estimation based on the slowest belt speed occurring in the operating range. Fig. 7 shows the resulting profiles of the suspension height and cake height for two different compartment resolutions. The absolute height of the suspension is not relevant for model predictive control or for local flow, as the influence of hydrostatic pressure is neglected in the model and the suspension height in the operating range under consideration is only a few millimeters.

However, a coarser spatial resolution results in a limited accuracy of locating the start of the desaturation zone. An inaccurate determination of this position means that the filter cake has a longer or shorter distance available for desaturation. This effect becomes increasingly significant as the compartment resolution decreases. A more detailed representation of the desaturation zone for a fixed operating condition as a function of compartment resolution is shown in Fig. 7. Simulations were

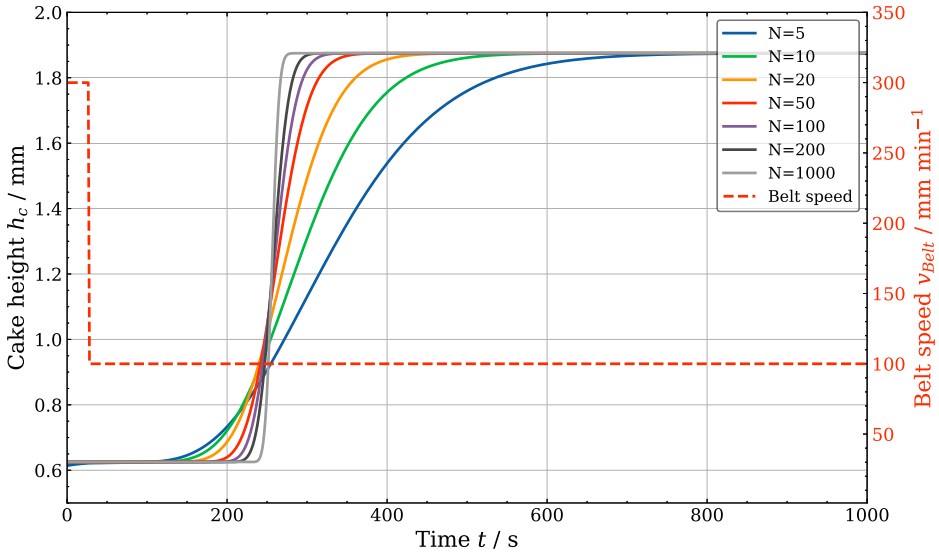

Fig. 6. Influence of the number of compartments N on the temporal course of the simulated filter cake height in the last compartment after a step change of belt speed from 300 mm min^{-1} to 100 mm min^{-1}. The simulations were performed with a constant suspension feed rate of $\dot{V}_{in}$= 50 ml min^{-1}, a solids volume fraction of c_V = 0.15, and identical model parameters.

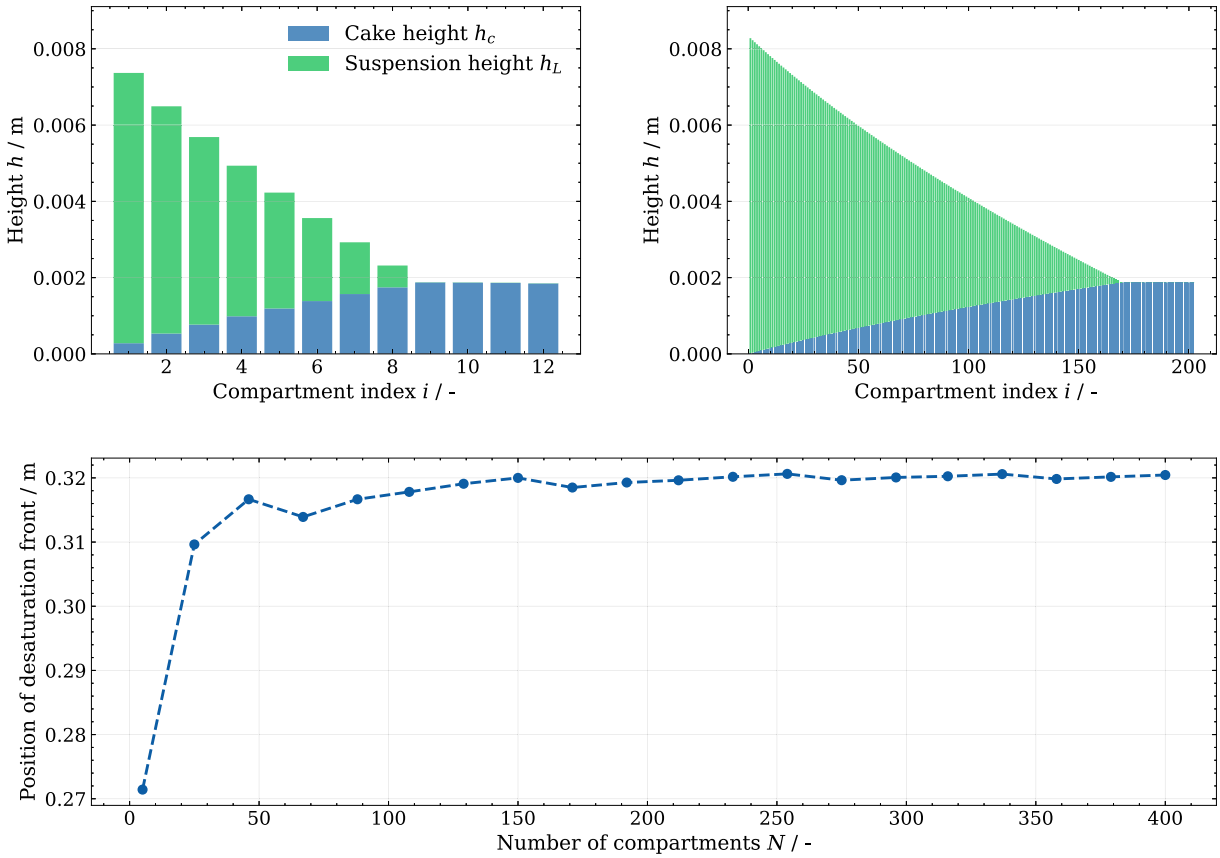

Fig. 7. Comparison of cake and suspension heights and the position of the desaturation zone at a constant CFL number of 0.1, v_{belt} = 100 mm min^{-1}, $\dot{V}_{in}$ = 50 ml min^{-1} and c_V = 15%. The top left shows the cakes and suspension heights along the belt for N = 12. The top right shows the corresponding height profiles for N = 200. The bottom shows the position of the transition point between filtration and desaturation as a function of the number of compartments N.

performed with the number of compartments ranging from 5 to 400. Even with 5 compartments and a time discretization of 10 s, the CFL number is 0.66 and is therefore in the stable convergence range. The maximum difference in the position of the mechanical dewatering zone is approximately five millimeters. From a resolution of 50 compartments, the deviation is less than one millimeter. Based on the reference solution with 400 compartments, this results in a relative deviation of less than 1 %, meaning that the solution can be considered converged as the number of compartments continues to increase.

4.3. Simulation and validation

The findings from Fig. 7 can now be used to simulate the cake height and residual moisture content of the filter cake for a compartment number of $N = 200$. Fig. 8 shows an example of the spatially progress of the cake formation process and subsequent desaturation along the belt length for one operating point. After a filter belt length of 210 mm, the suspension has completely drained into the filter cake, so that desaturation of the cake begins at this point. The desaturation zone extends over a length of 170 mm, corresponding to 44.7% of the effective filter belt length. At the transition to the desaturation zone, there is an abrupt drop in cake saturation, which turns into an asymptotic curve within a few millimeters and approaches equilibrium saturation. Noticeable is, that equilibrium is not reachable within the limited time frame of our belt configuration. Overall, it can be seen that approximately 92% of the total desaturation is already achieved within the first 3 mm of the desaturation zone. Conversely, around 98% of the desaturation zone is responsible for the remaining 8% of desaturation. However, these percentages and the sharp gradient are not universally valid, but result exclusively from the fit parameter $n = 3$ of the desaturation kinetics assumed here.

From this, it can be qualitatively deduced that, from a desaturation perspective, a higher suspension feed rate would be feasible. However, this is initially limited by the structural constraints of the test facility, which restrict a high feed rate and make operation difficult. The nonlinearity of desaturation along the desaturation zone observed in this work is qualitatively consistent with the results of the work by Liu et al. [50]. There, the authors show that the majority of dewatering is achieved in the early phase of the desaturation process, while extending the dewatering time has only a minor additional effect on the residual moisture. This confirms the findings here that most of the desaturation takes place within a few millimeters and that the further desaturation area has only a minor role in the process. This can also be seen from experiments. All residual moisture values measured in the varied parameter range according to Table 1 resulted in values between 12.3% and 15.3% by mass without clear correlations to the parameters. Based on the porosity and solid density from Table 1, the calculated saturation levels range from 0.32 to 0.38. According to Fig. 8, these values are within the simulation range and confirm the plausibility of the assumptions made. A similar trend is also evident when comparing desaturation to the air flow rate during desaturation in the *supplementary information*. Here, the air flow rate through the filter cake does not increase further after 10 s, indicating that a steady state has been reached. It can therefore be assumed that all filter cakes are in the range of the equilibrium saturation for the investigated states of the lab-scale vacuum belt filter. The further focus is therefore more on the cake height.

Simulations show the steady state that should be achieved with the assumptions on the belt filter. In order to compare the simulated values with measured values directly on the belt filter, the dynamics of the measured cake height and pressure difference for the starting range up to the steady state are therefore important. Fig. 9 shows an example of the measurement result of a validation test for the time course of the measured cake height and the pressure difference. At the beginning of the measurement, only the height of the unloaded filter belt is recorded. After about $t = 300$ s, a characteristic filter cake height is established. Although the operating parameters do not change during the measurement, the cake height shows temporal fluctuations even after signal smoothing. These are due to a slightly uneven feed and the resulting axial and lateral inhomogeneity of the filter cake. The observed fluctuations in cake height during steady-state operation should therefore not be interpreted as measurement artifacts, but rather as inherent process dynamics of a continuously operated belt filter. Steady-state operation is to be interpreted here in the statistical sense, where the mean value settles over time without a completely constant signal curve being achieved. This results in a comparatively large standard deviation for model validation, meaning that an evaluation based on time-averaged values is preferable to a comparison of individual points in time. The pressure curve shown in Fig. 9 can essentially be explained by the loading condition of the filter belt. At the beginning of the measurement, the pressure difference is low because large areas of the filter belt are not covered with suspension, resulting in an increased intake of foreign air. As the load on the belt increases, the pressure difference rises continuously and approaches a value of approximately 0.5 bar.

The pressure curve shows that a pressure difference of 0.5 bar can be expected in a steady state. However, pressure fluctuations in the belt filter still lead to deviations between modeled and actual filtration times and saturations. The filter cake height is not affected by the assumption of an incompressible cake with homogeneous and constant cake porosity. Fig. 10 shows the average measured cake height in a steady state and the corresponding simulated cake height. Since different measurement parameters are compared here, Table 2 provides an overview of the settings. The adjusted volume flow fluctuates depending on the preload of the silicone tube to transport the suspension with a peristaltic pump from feed tank to the belt filter, which is why the volume flow was measured again for each experiment and the actual value was adapted after calibration. The calibration is done gravimetrically with the density of fluid and solid.

The model quality increases as the deviation of the data points from the parity line decreases. Overall, there is a good agreement between simulations and experiments within the operating range. With a coefficient of determination of $R^2 = 0.741$, the model shows a basic suitability for describing the process behavior for the lab-scale belt filter, but exhibits relevant deviations. The remaining deviations can be explained, by the comparatively high noise level of the measuring system. In

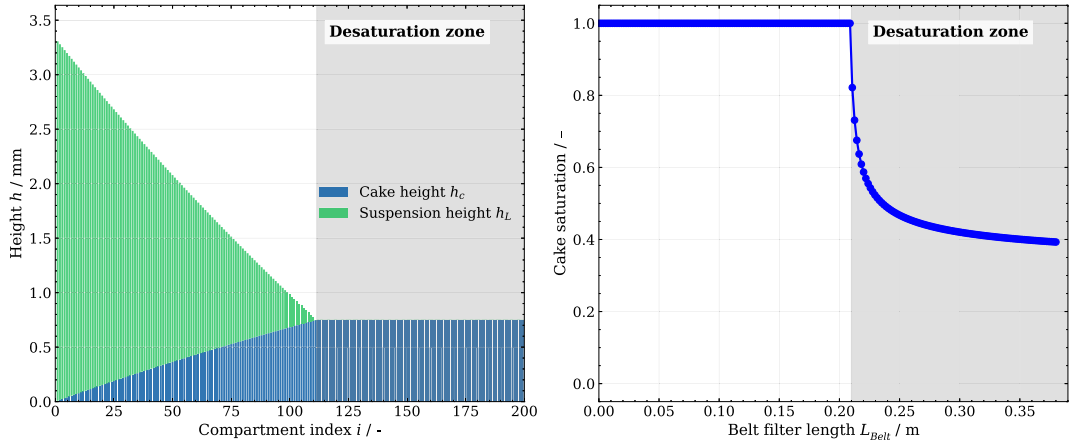

Fig. 8. Simulation of cake height and saturation along the filter belt in steady-state operation at $v_{belt} = 200$ mm min^{-1} and $\dot{V}_{in} = 40$ ml min^{-1}.

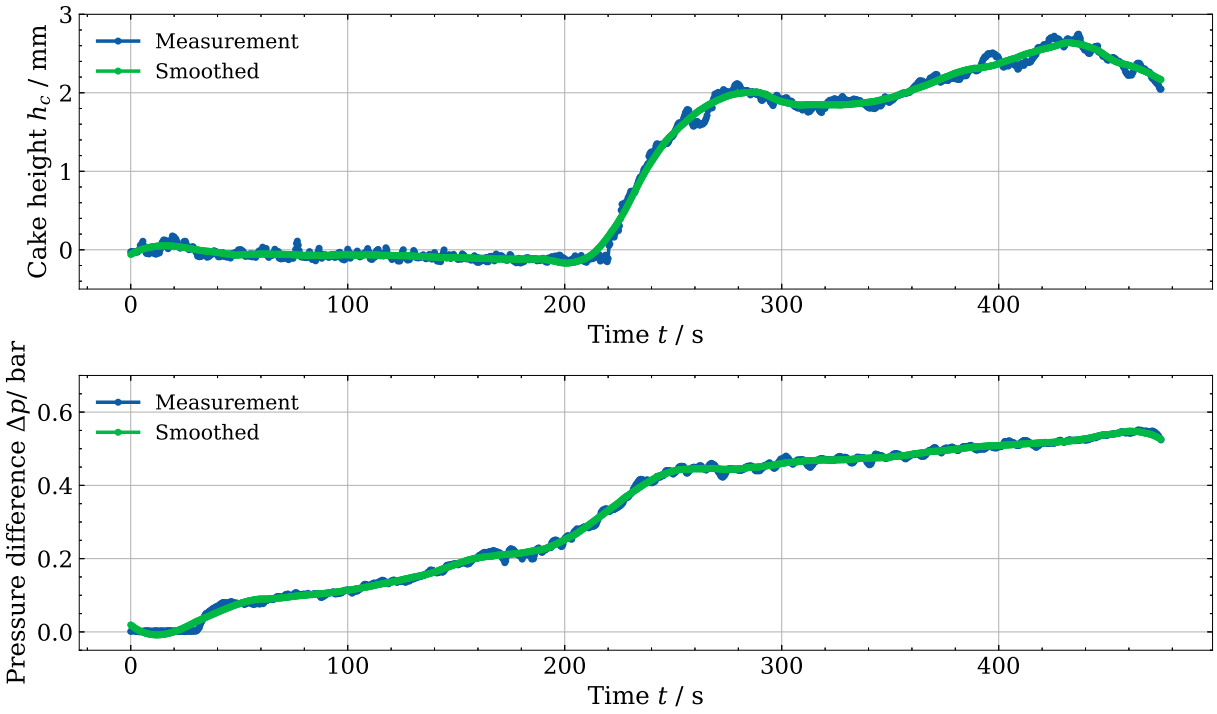

Fig. 9. Measurement results for height profile at the end of the belt filter (x = 380 mm) and pressure profile including smoothing. Operating conditions: $\dot{V}_{in}$ = 50 ml min^{-1}, v_{belt} = 100 mm min^{-1}, c_V = 15%.

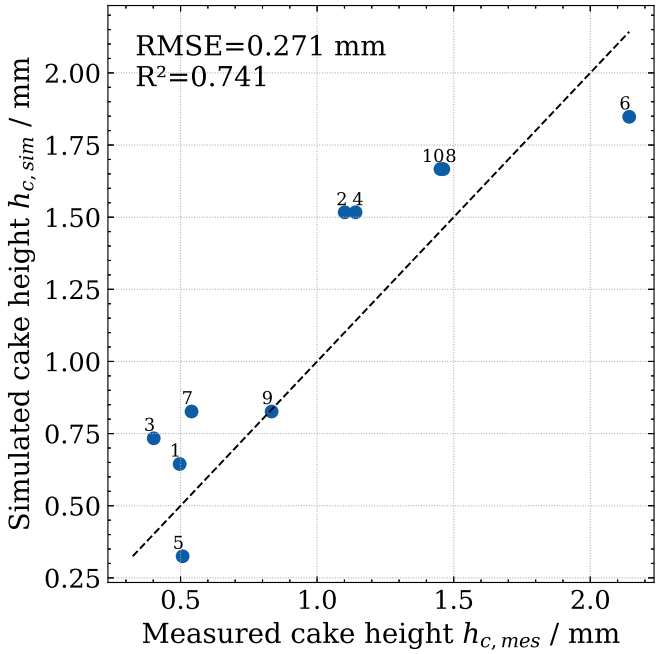

Fig. 10. Comparison of measured and simulated cake height for different operating conditions (Table 2). A parity plot with the ideal line is shown. The model quality is evaluated using the coefficient of determination R^2 and the root mean square error (RMSE).

relative terms, this influence is particularly pronounced at low cake heights, as the sensor resolution has a greater influence on the measurement in this case. As the cake height increases, the sensor noise becomes less significant. Instead, process-related effects such as inhomogeneous suspension feeding, edge effects on the filter belt, and uncertainties in parameter estimation dominate the model deviation. The model's computation time is another critical factor for real-time

Table 2
Overview of experimental tests with operating parameters and measured volume flow and cake height for model validation in Fig. 10.

Index	$\dot{V}_{in}$ / mL min^{-1}	v_{belt} / mm min^{-1}	c_V / %	h_c / mm
1	29.9	50	5	0.50
2	67.4	100	10	1.10
3	32.6	100	10	0.40
4	67.4	100	10	1.14
5	27.5	300	15	0.51
6	52.2	100	15	2.14
7	49.6	300	20	0.54
8	33.3	100	20	1.46
9	49.6	300	20	0.83
10	33.3	100	20	1.45

controlling capability. However, computation time depends on the specific architecture and the performance of the individual CPU/GPU. These simulations were run on an Intel Core i7-1065G7 CPU. At a resolution of N = 200 compartments, a single run took between 3.32 s and 3.67 s. With a minimum residence time of 76 s for the suspension on the belt filter, this corresponds to a simulation-to-process time ratio of 20:1. If a model predictive controller is additionally integrated, this time ratio decreases. Therefore, the computation time must be rechecked in the future after integration model predictive control to ensure stable process dynamics. While the Nyquist Theorem says only 2 times the highest sampling frequency is needed, practical controllers need 5 to 10 times to minimize phase lag and maintain stability [51]. Therefore, the model shows at the moment a useful agreement between simulated and measured parameters and is therefore suitable for future model predictive control developments.

5. Conclusion and outlook

This paper provides an optical measurement method using a camera that makes it possible to measure the transition from filtration to desaturation. The principle of this optical measurement is based on Beyerer

et al. [40]. Experiments have shown that, when comparing the bright-field and dark-field methods, only the bright-field method can deliver reliable results, which is in contrast to statements of Beyerer et al. [40] who mentions the dark field method to be more accurate. Particles also scatter the light, which means that the dark-field method does not detect any transition in light intensity. The application of the bright-field method to a video sequence proves its feasibility in a continuous process. Similar work is done by Huttunen et al. [52] who uses a thermographic camera to characterize the desaturation of filter cakes in vacuum filters. With a combination of his work with the result shown here, more information about the filtration process are detectable using the same equipment.

In addition to the optical measurement method, a multi-compartment model to describe the dynamic filtration behavior on a lab-scale vacuum belt filter was developed, which is based on the work of Gleiß et al. and Zhai et al. [30,31]. At this point, the vacuum belt filter is divided into two zones, the cake formation zone and the mechanical dewatering zone, with different physical behavior. The interconnection of compartments which allows to predict the temporal change of the filter cake height and the mechanical desaturation dependent on the belt length. The results show that the number of compartments influences the retention time behavior of the filter cake on the belt. A critical assumption is that no sedimentation occurs, since the particles have a density difference of a factor of 2.7 compared to the liquid. Therefore, this model cannot be directly applied to pilot belt filters, as the deviations in filtration from the model increase with increasing residence time. For A comparison between experimentally and simulatively determined cake heights shows that the differences have a coefficient of determination of $R^2 = 0.741$ and are therefore sufficient for a determination and estimation. With this verification, the next step to connect both systems of real-time measurement and model is possible and dynamic changes can be tested. A further combination of this work with Sauer et al. who simulated inhomogeneous filter cakes would help to enhance the belt filter model [29].

This work serves as the foundation for further research aimed at improving the prediction of cake formation and dewatering on vacuum belt filters. This includes predicting currently unknown parameters such as relative permeability, capillary pressure, and porosity from experimental data. However, predicting unknown material properties requires the integration of a parameter estimation framework. Another application of the presented model is the integration of the dynamic model with MPC to control the belt speed to reach an optimal minimum residual moisture content of the filter cake. This involves investigating the influence of the number of compartments on computation time, the integration of the aforementioned state estimation for unmeasurable variables and the defintion of constraints. Ultimately, it would be conceivable to achieve autonomous operation under fluctuating feed conditions by combining in-line measurement technology, modeling, and control. Additionally, it is conceivable to extend the presented model to other continuous vacuum filters such as drum filters, disc filters, and plate filters. For this purpose, the compartment model must be adapted to the geometry of these filter apparatuses.

Funding

The authors would like to thank the Deutsche Forschungsgemeinschaft (DFG, German Research Foundation) - Project number: 504852622 for funding the project in the priority program autonomous processes in particle technology SPP2364.

Declaration of generative AI and AI-assisted technologies

During the writing process of this work the authors used DeepL Write to examine sections of the manuscript for spelling and grammar. After using this tool, the authors reviewed and edited the content as needed and take full responsibility for the content of the publication.

Declaration of competing interest

The authors declare that they have no known competing financial interests or personal relationships that could have appeared to influence the work reported in this paper.

Acknowledgments

The authors would like to thank all colleagues and students for the support in research and writing of this paper.

Appendix A. Supplementary data

Supplementary data to this article can be found online at https://doi.org/10.1016/j.seppur.2026.138878.

Data availability

Data will be made available on request.

References

[1] H. Anlauf, Wet cake filtration: fundamentals, equipment, and strategies, Wiley-VCH, Weinheim, Germany (2019), https://doi.org/10.1002/9783527820665.
[2] C. Steenweg, A.I. Seifert, N. Böttger, K. Wohlgemuth, Process intensification enabling continuous manufacturing processes using modular continuous vacuum screw filter, Org. Process Res. Dev. 25 (2021) 2525–2536, https://doi.org/10.1021/acs.oprd.1c00294.
[3] P. Muñoz, A. Azevedo, R. Rodrigues, J. Rubio, Chemical pretreatment enhances vacuum filtration of slime-rich iron ore tailings, Miner. Eng. 240 (2026) 110155, https://doi.org/10.1016/j.mineng.2026.110155.
[4] Henry Darcy, Les Fontaines Publiques de la Ville de Dijon, Victor Dalmont 2 (1856).
[5] D.R. Sperry, The principles of filtration, Metall. Chem. Eng. 15 (1916) 198–203.
[6] D.R. Sperry, A new method of conducting filtration tests, Ind. Eng. Chem. 18 (1926) 276–278.
[7] B.F. Ruth, Studies in filtration IV nature of fluid flow through filter septa and its importance in the filtration equation, Ind. Eng. Chem. 27 (1935) 806–816.
[8] P.C. Carman, Fluid flow through granular beds, Transactions 15 (1937) 150–166.
[9] J. Kozeny, Ueber kapillare Leitung des Wassers im Boden, Sitzungsber Akad Wiss 136 (1927) 271–306.
[10] H.P. Grace, Structure and performance of filter media. I. The internal structure of filter media, AIChE J. 2 (1956) 307–315, https://doi.org/10.1002/aic.690020307.
[11] H.P. Grace, Structure and performance of filter media. II, Performance of filter media in liquid service, AIChE J. 2 (1956) 316–336, https://doi.org/10.1002/aic.690020308.
[12] F.M. Tiller, H.R. Cooper, The role of porosity in filtration: IV. Constant pressure filtration, AIChE J. 6 (1960) 595–601, https://doi.org/10.1002/aic.690060418.
[13] M. Shirato, M. Sambuichi, H. Kato, T. Aragaki, Internal flow mechanism in filter cakes, AICHE J. 15 (1969) 405–409, https://doi.org/10.1002/aic.690150320.
[14] F.M. Tiller, C.S. Yeh, The role of porosity in filtration. Part XI: filtration followed by expression, AIChE J. 33 (1987) 1241–1256, https://doi.org/10.1002/aic.690330803.
[15] M. Winkler, M. Gleiss, H. Nirschl, Soft sensor development for real-time process monitoring of multidimensional fractionation in tubular centrifuges, Nanomaterials 11 (2021) 1114, https://doi.org/10.3390/nano11051114.
[16] M. Gleiss, H. Nirschl, About modeling and optimization of solid bowl centrifuges, Kona Powder Part. J. 41 (2024) 58–77, https://doi.org/10.14356/kona.2024010.
[17] F. Concha, O. Bascur, Phenomenological model of sedimentation, in: Proc. 12th Int. Miner. Process. Congr. XII IMPC 4, 1977, pp. 29–46.
[18] F. Concha, M.C. Bustos, Theory of sedimentation of flocculated fine particles, Proc. Eng. Found. Conf. Flocculation Sediment. Consol. (1986) 275–284.
[19] Richard Buscall, Lee R. White, The consolidation of concentrated suspensions. Part 1: the theory of sedimentation, R, Soc. Chem. 83 (1987) 873–891.
[20] F.M. Auzerais, R. Jackson, W.B. Russel, The resolution of shocks and the effects of compressible sediments in transient settling, Camb. Univ. Press 195 (1988) 437–462.
[21] M.C. Bustos, F. Concha, R. Bürger, E.M. Tory, Sedimentation and thickening: phenomenological foundation and mathematical theory, Kluwer Acad, 1999.
[22] R. Bürger, K.H. Karlsen, On some upwind finite difference schemes for the phenomenological sedimentation–consolidation model, Springer 42 (2001) 145–166.
[23] R. Bürger, S. Evje, K.H. Karlsen, On strongly degenerate convection–diffusion problems modeling sedimentation–consolidation processes, Elsevier 247 (2000) 517–556, https://doi.org/10.1006/jmaa.2000.6872.
[24] R. Bürger, F. Concha, K.H. Karlsen, Phenomenological model of filtration processes: 1. Cake formation and expression, Chem. Eng. Sci. 56 (2001) 4537–4553, https://doi.org/10.1016/S0009-2509(01)00115-4.

[25] A.D. Stickland, R.G. De Kretser, P.J. Scales, One-dimensional model of vacuum filtration of compressible flocculated suspensions, AIChE J. 56 (2010) 2622–2631, https://doi.org/10.1002/aic.12194.
[26] A.D. Stickland, L.R. White, P.J. Scales, Models of rotary vacuum drum and disc filters for flocculated suspensions, AIChE J. 57 (2011) 951–961, https://doi.org/10.1002/aic.12310.
[27] F. Sauer, H. Henn, B. Hoffner, Predicting the wash behaviour of filter cakes with inhomogeneous cake geometry on a macroscopic scale, Chem. Eng. Sci. 299 (2024) 120484, https://doi.org/10.1016/j.ces.2024.120484.
[28] F. Sauer, H. Henn, U. Peuker, B. Hoffner, Experimental study on mechanical dewatering and displacement washing of filter cakes with inhomogeneous cake geometry, Sep. Purif. Technol. 349 (2024) 127904, https://doi.org/10.1016/j.seppur.2024.127904.
[29] F. Sauer, H. Henn, B. Hoffner, Modeling approach to mechanical gas dewatering of filter cakes with non-uniform cake height, Chem. Eng. Technol. 48 (2025) e202400353, https://doi.org/10.1002/ceat.202400353.
[30] M. Gleiss, S. Hammerich, M. Kespe, H. Nirschl, Development of a dynamic process model for the mechanical fluid separation in decanter centrifuges, Chem. Eng. Technol. 41 (2018) 19–26, https://doi.org/10.1002/ceat.201700113.
[31] O. Zhai, N. Ehret, F. Rhein, M. Gleiss, Enhancing decanter centrifuge process design with data-driven material parameters in multi-compartment modeling, J. Adv. Manuf. Process. 6 (2024) e10179, https://doi.org/10.1002/amp2.10179.
[32] H.K. Baust, S. Hammerich, H. König, H. Nirschl, M. Gleiß, Resolved simulation of the clarification and dewatering in decanter centrifuges, Processes 12 (2023) 9, https://doi.org/10.3390/pr12010009.
[33] S. Hammerich, M. Gleiß, M. Kespe, H. Nirschl, An efficient numerical approach for transient simulation of multiphase flow behavior in centrifuges, Chem. Eng. Technol. 41 (2018) 44–50, https://doi.org/10.1002/ceat.201700104.
[34] R. Boiocchi, C.R. Behera, A. Sherratt, C.T. DeGroot, K.V. Gernaey, G. Sin, D. Santoro, Dynamic model validation and advanced polymer control for rotating belt filtration as primary treatment of domestic wastewaters, Chem. Eng. Sci. 217 (2020) 115510, https://doi.org/10.1016/j.ces.2020.115510.
[35] D. Bourcier, J.P. Féraud, D. Colson, K. Mandrick, D. Ode, E. Brackx, F. Puel, Influence of particle size and shape properties on cake resistance and compressibility during pressure filtration, Chem. Eng. Sci. 144 (2016) 176–187, https://doi.org/10.1016/j.ces.2016.01.023.
[36] W. Brutsaert, The permeability of a porous medium determined from certain probability laws for pore size distribution, Water Resour. Res. 4 (1968) 425–434, https://doi.org/10.1029/WR004i002p00425.
[37] VDI, 2762 Part3: Mechanical solid-liquid separation by cake filtration - Mechanical deliquoring of incompressible filter cakes by undersaturation using a gas pressure difference, 2017.
[38] M. Hamachi, M. Mietton-Peuchot, Cake thickness measurement with an optical laser sensor, Chem. Eng. Res. Des. 79 (2001) 151–155, https://doi.org/10.1205/02638760151095962.
[39] M. Haenecke, Lasertriangulationsmessung der zeitlichen Änderung der Staubkuchendicke an flexiblen Filtermedien zur Validierung numerischer Simulationen, Bergische Universität Wuppertal (2021), https://doi.org/10.25926/J94S-7W13.
[40] J. Beyerer, F. Puente León, C. Frese, J. Meyer, Automatische Sichtprüfung: Grundlagen, Methoden und Praxis der Bildgewinnung und Bildauswertung, 2. Aufl. 2016, Springer Berlin 2016, 2016, https://doi.org/10.1007/978-3-662-47786-1.
[41] V.D.I. VDI, 2762 Part 2. Mechanical solid-liquid separation by cake filtration. Determination of filter cake resistance, 2010.
[42] H. Liu, Y. Huang, Z. Liu, L. Dong, M. Wang, The development and application of novel water-based drilling fluid for complex pressure system formation in the South China Sea, Processes 11 (2023) 1323, https://doi.org/10.3390/pr11051323.
[43] I.M. Hauner, A. Deblais, J.K. Beattie, H. Kellay, D. Bonn, The dynamic surface tension of water, J. Phys. Chem. Lett. 8 (2017) 1599–1603, https://doi.org/10.1021/acs.jpclett.7b00267.
[44] C.R. Harris, K.J. Millman, S.J. Van Der Walt, R. Gommers, P. Virtanen, D. Cournapeau, E. Wieser, J. Taylor, S. Berg, N.J. Smith, R. Kern, M. Picus, S. Hoyer, M.H. Van Kerkwijk, M. Brett, A. Haldane, J.F. Del Río, M. Wiebe, P. Peterson, P. Gérard-Marchant, K. Sheppard, T. Reddy, W. Weckesser, H. Abbasi, C. Gohlke, T.E. Oliphant, Array programming with NumPy, Nature 585 (2020) 357–362, https://doi.org/10.1038/s41586-020-2649-2.
[45] P. Virtanen, R. Gommers, T.E. Oliphant, M. Haberland, T. Reddy, D. Cournapeau, E. Burovski, P. Peterson, W. Weckesser, J. Bright, S.J. Van Der Walt, M. Brett, J. Wilson, K.J. Millman, N. Mayorov, A.R.J. Nelson, E. Jones, R. Kern, E. Larson, C. J. Carey, İ. Polat, Y. Feng, E.W. Moore, J. VanderPlas, D. Laxalde, J. Perktold, R. Cimrman, I. Henriksen, E.A. Quintero, C.R. Harris, A.M. Archibald, A.H. Ribeiro, F. Pedregosa, P. Van Mulbregt, et al., 1.0: fundamental algorithms for scientific computing in Python, Nat. Methods 17 (2020) 261–272, https://doi.org/10.1038/s41592-019-0686-2.
[46] Gesellschaft Verfahrenstechnik und Chemieingenieurwesen, Verein deutscher Ingenieure, eds., VDI-Wärmeatlas: VDI, 11. bearb. und erw. Aufl, Springer Vieweg, Berlin [u.a.], 2013, https://doi.org/10.1007/978-3-642-19981-3.
[47] L. Hamraoui, A. Bergani, M. Ettoumi, A. Aboulaich, Y. Taha, A. Khalil, C. M. Neculita, M. Benzaazoua, Towards a circular economy in the mining industry: possible solutions for water recovery through advanced mineral tailings dewatering, Minerals 14 (2024) 319, https://doi.org/10.3390/min14030319.
[48] J.H. Ferziger, Numerische Strömungsmechanik, Springer, Berlin / Heidelberg, Berlin, Heidelberg, 2008.
[49] C.G. Hill, T.W. Root, Introduction to Chemical Engineering Kinetics and Reactor Design, Second edition, Wiley, Hoboken, New Jersey, 2014.
[50] H. Liu, K. You, Optimization of dewatering process of concentrate pressure filtering by support vector regression, Sci. Rep. 12 (2022) 7135, https://doi.org/10.1038/s41598-022-11259-9.
[51] N. Hori, R.U. Newton, N. Kawamori, M.R. McGuigan, W.J. Kraemer, K. Nosaka, Reliability of performance measurements derived from ground reaction force data during countermovement jump and the influence of sampling frequency, J. Strength Cond. Res. 23 (2009) 874–882, https://doi.org/10.1519/JSC.0b013e3181a00ca2.
[52] M. Huttunen, L. Nygren, T. Kinnarinen, B. Ekberg, T. Lindh, V. Karvonen, J. Ahola, A. Häkkinen, Real-time monitoring of the moisture content of filter cakes in vacuum filters by a novel soft sensor, Sep. Purif. Technol. 223 (2019) 282–291, https://doi.org/10.1016/j.seppur.2019.03.091.